PAPER

Check for updates

Promoting solution-phase superlattices of CsPbBr₃ nanocrystals

Noel Mireles Villegas, [ID] [a] Josue C. Hernandez, [ID] [a] Joshua C. John [ID] [b] and Matthew Sheldon [ID] *[a,b]

We present a size-selective method for purifying and isolating perovskite CsPbBr₃ nanocrystals (NCs) that preserves their as-synthesized surface chemistry and extremely high photoluminescence quantum yields (PLQYs). The isolation procedure is based on the stepwise evaporation of nonpolar co-solvents with high vapor pressure to promote precipitation of a size-selected product. As the sample fractions become more uniform in size, we observe that the NCs self-assemble into colloidally stable, solution-phase super-lattices (SLs). Small angle X-ray scattering (SAXS) and dynamic light scattering (DLS) studies show that the solution-phase SLs contain 1000s of NCs per supercrystal in a simple cubic, face-to-face packing arrangement. The SLs also display systematically faster radiative decay dynamics and improved PLQYs, as well as unique spectral absorption features likely resulting from inter-particle electronic coupling effects. This study is the first demonstration of solution-phase CsPbBr₃ SLs and highlights their potential for achieving collective optoelectronic phenomena previously observed from solid-state assemblies.

Introduction

Recent progress in the synthesis of high-quality perovskite semiconductor nanocrystals (NCs) with the chemical stoichiometry CsPbX₃ (X = Cl, Br, or I), has led to significant interest for their use as the optoelectronic components in technologies such as photovoltaics,[4–6] LEDs[7–10] and thermal-to-optical energy converters.[11–15] For these applications the colloidal NCs must be isolated from the solvent phase and deposited as films in solid state device platforms, while preserving the near-unity photoluminescence quantum yield (PLQY) and minimal electronic trap states that characterizes an optimized synthetic preparation. During processing and film deposition it has been observed that CsPbX₃ NCs can be assembled into super-lattices (SLs) in which the cuboid nanoparticles form well-ordered, μm-sized aggregates with cubic, face-to-face stacking that extends in all three spatial dimensions.[3,16] The SL geometry promotes enhanced inter-particle electronic coupling, giving rise to unique optoelectronic properties as a result of the more delocalized electronic structure.[17–19] The observation of superfluorescence (SF),[1,20,21] long exciton diffusion lengths,[18] and extended exciton coherence times[22,23] has led researchers to investigate how to optimally promote the self-assembly of SLs for applications in electrical-to-optical modu-

lators,[24] spectrally ultra-pure laser sources,[25] and quantum computing.[26–28] Notably, to date, these electronic coupling effects have only been observed in solid-state assemblies at cryogenic temperatures below 10 K.[1,20,21] However, better control of the SL structure may allow for preservation of these unique collective electronic phenomena even at room temperature.[25,29]

The overriding challenge for preparing SLs from NCs is the requirement of precise control over the ordering of matter at the atomic, nano- and mesoscale *via* self-assembly. Many different classes of colloidal NC materials have been shown to organize into SLs *via* a general strategy of controllably modulating interactions between NCs as they are transferred from the solvent phase to the solid-state.[30–33] Several interrelated factors such as the NC composition, size, and surface chemistry, as well as characteristics of the environment such as solvent polarity, temperature, or externally applied fields entail that the ideal conditions are a complex optimization that is unique for each materials system.[33–35] Slow solvent evaporation in combination with destabilization of the colloid suspension, often by perturbing the surfactant ligand chemistry or solvent polarity, is commonly employed to promote a time-controlled inter-particle contraction process.[36,37] This must be carried out with extremely uniform distributions of the underlying NC dimensions to result in SLs with macroscopic dimensions.

Nevertheless, these strategies have met with limited success for CsPbX₃ NCs primarily due to challenges maintaining structural and chemical stability during their processing and deposition. The generally poorer stability of CsPbX₃ in comparison

[a] Department of Chemistry, Texas A&M University, College Station, Texas 77842, USA. E-mail: sheldonm@tamu.edu
[b] Department of Material Science and Engineering, Texas A&M University, College Station, Texas 77840, USA

with other classes of colloidal NCs is a well-known issue. The ionic lattice and relatively soft mechanical properties result in low crystal energy, such that $CsPbX_3$ NCs decompose in polar solvents or in ambient conditions with trace humidity.[38] Weak and dynamic surface ligand binding further undermines colloidal stability and can lead to uncontrolled agglomeration and recrystallization of the NCs as the surface ligand shell is easily disrupted during conventional processing protocols.[39,40] Typically, the crude product of a NC synthesis is isolated and purified by centrifugation after the addition of polar solvents to destabilize the colloid suspension. The undesirable consequence for $CsPbX_3$ NCs is ligand stripping that introduces surface electronic defects and decreased PLQY, as well as NC recrystallization that disrupts the size uniformity necessary for successful self-assembly.[41–43]

To address challenges related to post-synthetic processing, we have developed a method for isolating and concentrating size-selected fractions of $CsPbBr_3$ NCs that provides exceptional preservation of their electronic and structural integrity. The key distinguishing feature is the intentional lack of polar solvents during cleaning and precipitation. Instead, two miscible non-polar solvents with high and low vapor pressure, hexane and 1-octadecene (1-ODE) respectively, are used to suspend the colloid. Multiple product fractions of $CsPbBr_3$ NCs are obtained by performing a stepwise selective evaporation of hexane, concentrating the NC product in the remaining 1-ODE, followed by centrifugation (Fig. 1(a)). Analysis of the size distribution functions of the purified NC products by dynamic light scattering (DLS) indicates a continuous decrease in the average NC size and focusing of the NC size distribution within each subsequent isolated fraction. Remarkably, in combination with structural analysis of the resuspended NC product using small angle X-ray scattering (SAXS), we find that the purification steps promote solution-phase, simple cubic SLs with ~1000–8000 NCs per supercrystal. The appearance of solution-phase SLs is correlated with clear evidence for interparticle electronic coupling effects in the absorption spectrum. Additionally, we observe a systematic increase in the PLQY and corresponding decrease in photoluminescence lifetime with each additional purification step. Our findings suggest that when $CsPbBr_3$ NCs are well-ordered into colloidally stable SLs their optoelectronic response is further improved by inter-particle electronic coupling effects.

Experimental

Chemicals

Cs_2CO_3 (99.9%), PbO (99%), oleic acid (OA, 90%), oleylamine (OAm, 70%), 1-octadecene (ODE, 90%) and hexane (95%) were received from Sigma-Aldrich. $PbBr_2$ (98+%) was purchased from Alfa Aesar.

Synthesis of $CsPbBr_3$ NCs

A 25 mL 2-neck round bottomed flask was filled with Cs_2CO_3 (0.200 g), 1-ODE (10 mL), and OA (1 mL). The mixture was

heated at 110 °C for 1 hour to obtain Cs-oleate. The resulting solution was then subjected to three cycles of vacuum flushing to remove trace gas byproducts. A 3-neck round bottom flask was filled with $PbBr_2$ (0.060 g) and 1-ODE (5 mL) to form the lead halide precursor solution. This solution was heated at 120 °C under high vacuum for 1 hour. OAm and OA ligands were prepared by heating at 110 °C in glass vials equipped with septa caps, followed by three cycles of vacuum-to-argon flushing to remove trace water and gas byproducts. The Cs-oleate flask and the $PbBr_2$ precursor solution were then placed under argon. The temperature of the Cs-oleate flask was increased to 150 °C, and the temperature of the $PbBr_2$ solution was increased to 180 °C, OAm (0.5 mL) was injected into the $PbBr_2$ precursor solution using a syringe, followed by the addition of OA (0.5 mL). The solubilization of $PbBr_2$ was confirmed by the appearance of a clear and faint-yellow solution. The Cs-oleate precursor (0.4 mL) was swiftly injected into the solubilized $PbBr_2$ precursor solution at 180 °C. The reaction mixture was immediately quenched using an ice-bath.

Fractioning methods

The crude reaction product was centrifuged at 3000g-forces for 10 min. The supernatant was discarded, and the precipitate was resuspended in 4 mL of hexane and centrifuged again for 5 min at 3000g-forces. The resulting supernatant was transferred to a clear vail, and a small portion was set aside for analysis as the starting "Parent NC." 3 mL of 1-ODE was added to the rest of the supernatant, resulting in the formation of a cloudy and yellow precipitate that was isolated by centrifugation for 8 minutes at 3000g-forces. This precipitate was designated as "Fraction 1," and the remaining supernatant was transferred to a clear vial with a septa cap. Argon gas was supplied to one of the needles punctured through the septa to evaporate hexane from the solution, while the other needle allowed the escape of all gas. The evaporation cycle was repeated until all hexane was evaporated, with each cycle starting with a clear, bright green suspension and ending with the formation of a yellow, cloudy precipitate that was separated by centrifugation at 3000g-forces for 8 minutes and designated as an isolated fraction. On average, six product fractions were obtained and the left-over supernatant from final precipitation was composed of NCs in pure 1-ODE and was kept and labeled as "1-ODE NC."

Characterization

Transmission electron microscopy (TEM) images were taken using an FEI Tecnai G2 F20 ST FE-TEM operated at an accelerating voltage of 200 kV equipped with a Gatan CCD camera. Scanning electron microscope (SEM) images were taken using an FEI Helios NanoLab 460F1 DualBeam Focused Ion Beam (FIB)-SEM with secondary electrons (SE) at a current of 3.1 pA and using a low voltage electron beam (HV = 2 kV) to minimize charging. Absorption and photoluminescence spectra were collected on an Ocean Optics Flame-S UV-vis spectrometer with an Ocean Optics DH-2000-BAL deuterium and halogen lamp as the light source. The relative scattering measurements were
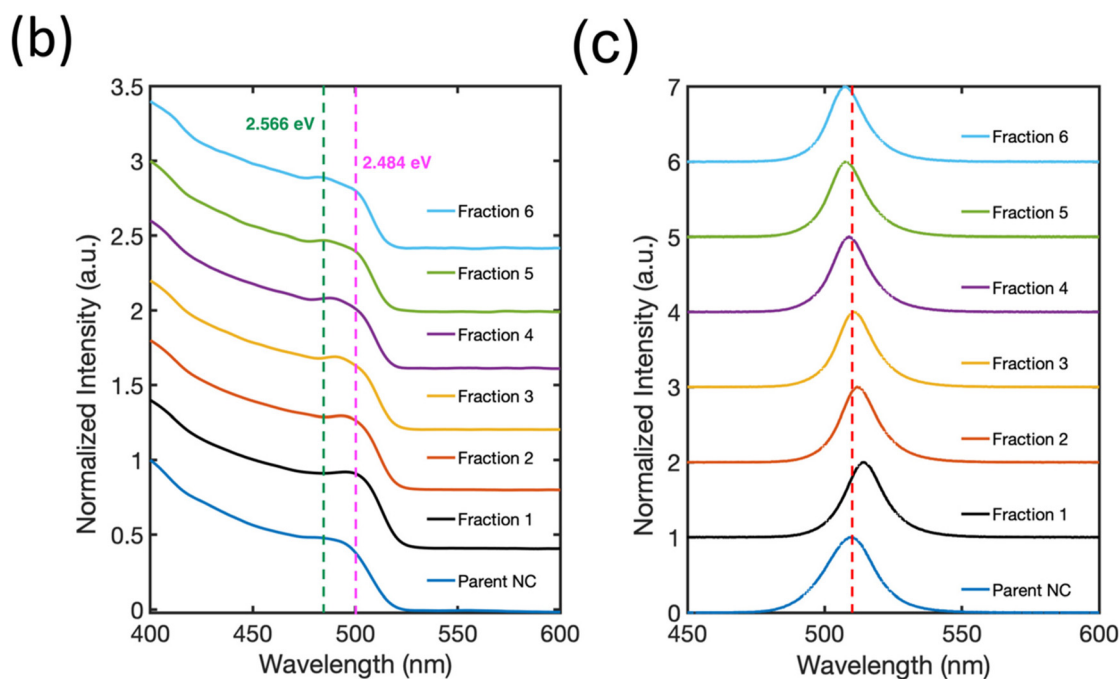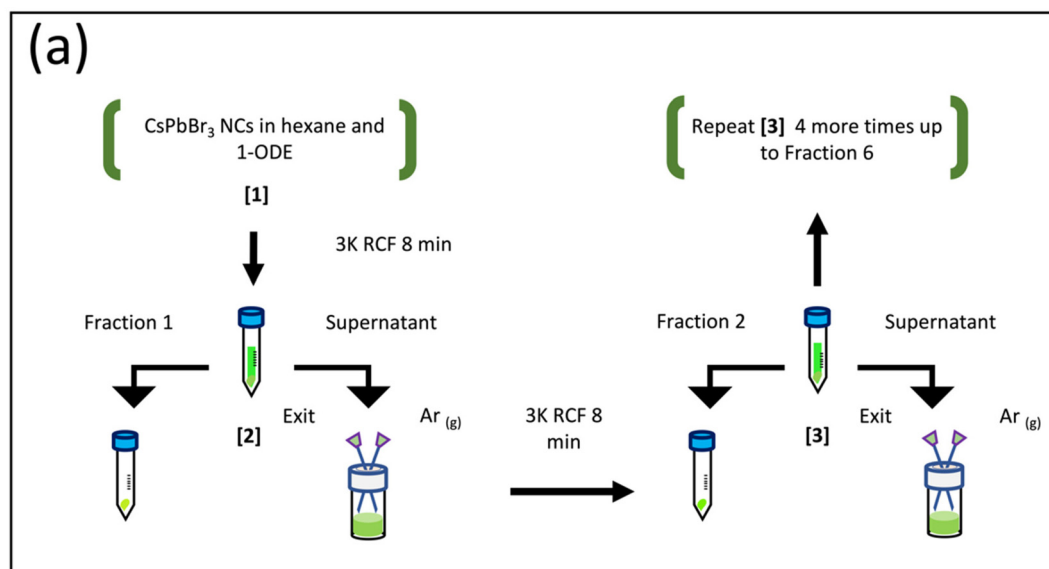
Fig. 1 (a) Size-selective NC isolation by the stepwise evaporation of hexane from the colloid mixture. (b) Absorption spectra of Parent NCs and Fractions 1–6 shifted on the y-axis for ease of comparison. The prominent energy states in Fraction 6 are indicated by the green (2.566 eV) and pink (2.484 eV) dotted lines. (c) PL spectra of Parent NCs and Fractions 1–6. The PL maximum of the Parent NCs is indicated by the red dotted line centered at 510 nm.

performed using a pulsed white laser (NKT Photonics, SUPERK FIANIUM, FIR-15) coupled with a laser line tunable filter (LLTF) from Photon Etc. (LLTF CONTRAST VS-2) with the excitation source centered at 420 nm. An Ocean Optics Flame-S UV-vis spectrometer was placed perpendicular to the path of incidence to collect both the emission and the scattered excitation. Powder XRD measurements were performed using a Bruker-AXS D8 Advanced Bragg–Brentano Diffractometer with a Cu Kα radiation source ($\lambda = 1.5418$ Å). Photoluminescence lifetime was recorded under 80 ps pulsed excitation at 405 nm

(PicoQuant, P-C 405) with a time-correlated single photon counting instrument (PicoHarp 300) and an avalanche photo-diode (MPD PDM series) for detection. Absolute PLQY measurements were collected using an integrating sphere (Gigahertz-Optik, UPB-150-ARTA) equipped with a monochromator (Sciencetech, 9055-monochromator, grating 631-0037, 1200 l mm^{-1}@500 nm) and a single channel detector (Sciencetech, S-025-TE2-H) using a pulsed white laser (NKT Photonics, SUPERK FIANIUM, FIR-15) coupled with a laser line tunable filter (LLTF) from Photon Etc. (LLTF CONTRAST

VS-2) for excitation source. The Malvern Zeta sizer (Nano Series, Nano ZS) instrument was used to determine the hydro-diameter in the dynamic light scattering (DLS) experiments. SAXS data was measured on a Rigaku-S-MAX 3000 three-pinhole collimator system with rotating anode generator X-ray source (MicroMax-007 HF) and 2D configurable detector. The samples were measured inside 1.5 mm quartz flow cell capillary.

Results and discussion

Methodology

$CsPbBr_3$ NCs were synthesized by following the protocol of Roman *et al.*[13] The crude reaction product of "Parent NCs" was precipitated and then resuspended in hexanes with 1-ODE added as a cosolvent for the size-selective fractioning process, summarized by the schematic shown in Fig. 1(a). Upon 1-ODE addition, a yellow and cloudy precipitate formed and was separated from solution. This initial precipitate was termed as "Fraction 1." Each subsequent fraction was isolated step-wise by repeating a cycle that started by evaporating hexane with Ar gas, and then centrifuging. Before hexane evaporation, the sample is a clear and bright green suspension. Evaporation is continued until the formation of a cloudy and yellow precipitate, followed by centrifugation and resuspension of the precipitate in hexane. The remaining supernatant undergoes further processing by repeating the same procedure until all of the hexane is evaporated, and multiple fractions are collected. The total number of sample fractions obtained is dependent on the concentration of the Parent NC suspension. For a given synthesis, an average of six product fractions were isolated and resuspended in hexanes to a final ~0.80 μM concentration each, as determined by UV-Vis absorption. Fraction 5 and Fraction 6 were the lowest yield product fractions. More details of the synthesis and fractioning process are available in the Experimental section. Note that Fraction 1 was obtained prior to any hexane evaporation and comprises the most colloidally unstable NCs that are present in the starting colloid. Transmission electron microscopy (TEM) images, as shown in Fig. 2, reveal a marked improvement in NC shape and size achieved by the isolation and purification process leading to Fraction 6. We have achieved similar results for isolating $CsPbCl_3$ and $CsPbI_3$ NCs synthesized through similar methods. We suspect our method can be extended to other perovskite systems with similar NC surface chemistry since 1-ODE and hexane are commonly used solvent systems for these materials.

Fig. 1(b) shows the absorption curves of the fractions and Parent NC suspensions shifted on the *y*-axis for ease of comparison. Compared with the Parent NCs, there is a minor improvement in the definition of the lowest energy exciton absorption feature around 2.484 eV (pink dotted line) for Fraction 2. For each subsequent fraction (Fig. 1(b)), splitting of the exciton absorption feature into two electronic states becomes prominent, with the energy separation between these states increased with each fraction. By Fraction 6, the two
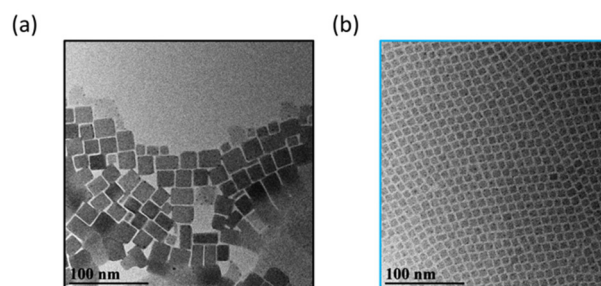

Fig. 2 (a) TEM image of Fraction 1 shows recrystallization of NCs giving rise to greater variation as well as oriented attachment and recrystallization at NC corners. (b) In contrast, the TEM image of Fraction 6 depicts uniformly sized NCs.

states give clear absorption features (Fig. 1(b)) at 2.566 eV (green dotted line) and 2.484 eV (pink dotted line). The samples show well-defined, symmetric photoluminescence emission spectra (Fig. 1(c)). The emission energy of Fraction 1 is red-shifted from the Parent NC since this fraction is made of the largest particles as seen by TEM in Fig. 2(a). The photoluminescence emission energy is continuously blue-shifted for Fractions 2–6, suggesting NCs of smaller dimensions with stronger quantum confinement effects for each subsequent fraction.

We used TEM to study the morphology of the NC fractions by diluting 1 drop of the stock solutions in 20 drops of hexanes. The diluted concentration ensured that individual NCs could be imaged. TEM images of Fraction 1 (Fig. 2(a)) revealed significant damage to the NC morphology manifest as corner-sharing NCs due to large-scale recrystallization. This oriented recrystallization and regrowth process is commonly observed in perovskite materials.[43–46] In Fig. 3, TEM images of Fractions 2–6 and the Parent NCs are displayed as insets. Product Fractions 2–6 show cuboidal morphology, but the structural quality and uniformity improved significantly in the later fractions. The early fractions were characterized by large NCs with larger size variations, whereas the later fractions showed smaller, more uniformly sized NCs. Fractions 2 and 3 showed minor morphological damage due to oriented attachment and recrystallization at NC corners, similar but less pronounced than that observed in Fraction 1 (Fig. 2(a)). No such damage was found in Fractions 4, 5, and 6, indicating that smaller NCs in the later fractions have better colloidal stability.

Determining size-distribution functions of isolated fractions by DLS

To better understand the electronic structure indicated by the optical spectra, we analyzed the statistics of the NC sizes, *i.e.*, the sample polydispersity. Our results rule out the possibility that a bimodal size distribution of NCs in the isolated fractions gave rise to the two different excitonic absorption features reported in Fig. 1(b). The size distribution functions of Parent NCs and the isolated fractions were obtained by per-
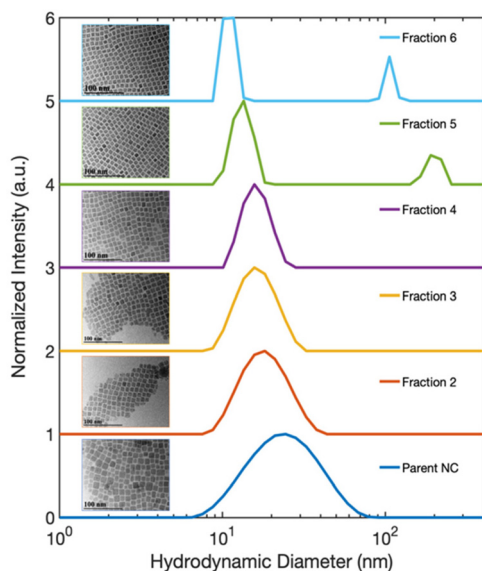
Fig. 3 The size distribution functions obtained by DLS indicate the hydrodynamic diameter of species in solution. The major feature corresponds to the diameter of isolated NCs which become smaller and more monodisperse with subsequent fractioning. The secondary peak with larger diameter in Fraction 5 and 6, corresponds to CsPbBr$_3$ SLs. TEM images of Fractions 2–6 and the Parent NCs are displayed as insets.

sistent with the continuously blue-shifted emission energy observed for each subsequent fraction in Fig. 1(c). In addition, a significant size focusing effect was observed. The monodispersity of Fraction 6 (Fig. 3, light blue trace) was improved by a factor of 10 compared to the Parent NC (Fig. 3, dark blue trace) as indicated by the full-width at half-maximum (FWHM) of the primary feature, termed "peak 1", in the size distribution function. The diameter associated with peak 1 corresponds to free, isolated NCs in solution, and matches the diameters of individual NCs observed under TEM. Additionally, the size distribution functions for Fractions 5 and 6 show a second signal with a much larger diameter, labeled "peak 2". This second feature corresponds to the SLs formed in solution, as further confirmed by SAXS (Fig. 4) studies detailed below. The SLs have an average diameter of 200 nm and 100 nm for Fraction 5 and 6, respectively. A quantitative summary of the parameters obtained from the size distribution functions is shown in Table 1. Importantly, the DLS data show that the splitting of

Table 1 Summary of average hydrodynamic diameter and FWHM of the major (peak 1) and minor (peak 2) in the DLS data in Fig. 3

Sample	Peak 1 max. (nm)	Peak 1 FWHM (nm)	Peak 2 max. (nm)	Peak 2 FWHM (nm)
Parent NC	24	44	—	—
Fraction 2	18	16	—	—
Fraction 3	16	12	—	—
Fraction 4	16	8	—	—
Fraction 5	15	5	203	63
Fraction 6	13	3	106	16

forming DLS experiments. The DLS measurement determines the average hydrodynamic diameter of particles in solution. The DLS results (Fig. 3) show a decrease in the average diameter with increasing fraction number. This decrease is con-
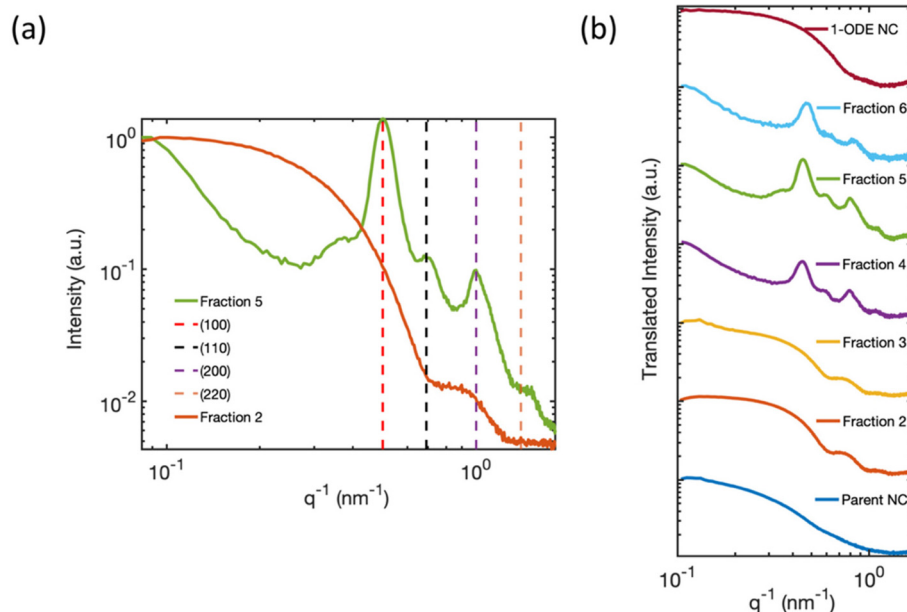

Fig. 4 (a) Solution-phase SAXS pattern of Fraction 2 and Fraction 5 measured inside a capillary tube. The SAXS pattern of Fraction 5 (green trace), is index matched with a simple cubic superlattice corresponding to a SL constant of 12.6 nm. The decreasing slope at small q^{-1} in Fraction 5 originated from mesoscale SLs with an average size greater than 90 nm, beyond the length scale limit of detection. The SAXS pattern of Fraction 2 (orange trace) is consistent with isolated 8–10 nm cuboidal CsPbBr$_3$ NCs.[1,2] (b) Summary of the solution-phase SAXS pattern of Parent NCs, Fractions 2–6, and 1-ODE NC sample (maroon trace). The SAXS patterns are offset on the y-axis for ease of comparison.

the excitonic absorption features (Fig. 1(b)) is more pronounced when the uniformity of the NCs is improved, and the absorption feature is clearly correlated with the formation of SLs in solution.

Structural analysis by SAXS and XRD

To uncover the 3D-structural information of the large-scale structures in the DLS signal, we measured the SAXS patterns of solution-phase suspensions of the isolated fractions inside capillary tubes. Fig. 4(a) compares the solution phase SAXS pattern of Fraction 2 and Fraction 5. The SAXS pattern of Fraction 2 is consistent with previous reports of highly monodisperse $CsPbBr_3$ NCs, with an average cube-edge length of 8–12 nm.[1,2] A broad, decreasing slope at small q^{-1} values indicates non-interacting and freely dispersed NC in solution.[47] Additionally, the steep decline in the slope at low q^{-1} values for Fraction 5 suggests that the NCs were no longer freely dispersed and had formed larger structures greater than 90 nm in size.[2,48,49] More precise estimate of the size of the structure is not possible based on the detection limit of our SAXS instrument. The large structure was highly crystalline, with Bragg reflection peaks identified at 0.50 nm^{-1}, 0.69 nm^{-1}, and 1.39 nm^{-1} q^{-1} values. These peaks match well with the (100), (110), and (200) lattice planes of a simple cubic ordered SL. The strongest Bragg reflection at 0.50 nm^{-1} corresponds to a SL lattice constant, i.e., the periodic spacing of individual NCs in the SL, of 12.6 nm, which was consistent with the distance measured in the TEM image of Fraction 5 (Fig. 3 inset image). Fractions 4 and 6 showed similar Bragg peaks, but with slightly shifted q^{-1} values due to differences in the average NC particle size. The first fraction for which SL formation was observed varied from batch to batch depending on the quality of the Parent NC solution. However, SLs are typically observed staring at Fraction 4 and are always observed in Fractions 5 and 6. We can therefore confirm that the large-diameter signals in the DLS (Fig. 3) studies for Fractions 5 and 6 are due to the presence of significant numbers of SLs in solution. Fig. 4(b) summarizes all collected SAXS patterns for the fractions and the starting Parent NC suspension, allowing for visual comparison. The Parent NC (Fig. 4(b), dark blue trace) was composed of polydispersed and non-interacting NCs, as indicated by the broad slope at small q^{-1} values and absence of Bragg scattering from crystallographic planes.

The SAXS pattern of the NCs that did not precipitate during the hexane evaporation process, and which remained in the pure 1-ODE supernatant, was also collected. This remaining supernatant, after all other fractions had been isolated, is referred to as 1-ODE NC. The SAXS pattern for 1-ODE NC (Fig. 4(b), maroon trace) showed no evidence of NC–NC interactions or mesoscale ordering. Instead, the scattering pattern was most closely related to that of the early fractions and the Parent NC (Fig. 4(b), dark blue trace), indicating the NCs that remained in the 1-ODE supernatant were freely dispersed. We then compared the absorption and photoluminescence spectra of the 1-ODE NC sample with that of Fraction 6 (Fig. 5). The comparison is provided, because these samples
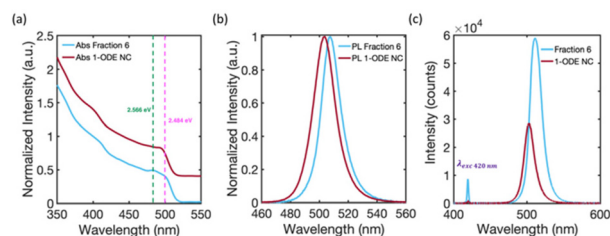

Fig. 5 (a) Absorption spectra comparison of Fraction 6 (blue trace) and of the NCs in the 1-ODE NC sample (maroon trace), and (b) corresponding PL spectra. The prominent energy states in Fraction 6 are indicated by the green (2.566 eV) and pink (2.484 eV) dotted lines. (c) PL spectra for Fraction 6 (blue trace) and 1-ODE NC (maroon trace) at equal concentrations under 420 nm excitation, demonstrating increased scattering of Fraction 6 due to the presence of SLs.

show photoluminescence emission at an energy that is more similar than any other fraction, suggesting the closest similarity in size. The peak photoluminescence emission for the 1-ODE NC sample was slightly blue-shifted and centered at 503 nm, compared to that of Fraction 6, which was centered at 507 nm. Despite being more quantum-confined than Fraction 6, the band-edge absorption structure of the 1-ODE NC sample (Fig. 5(a), maroon trace) did not show the same splitting of the excitonic feature observed in Fig. 5 (Fig. 5(a), light blue trace, splitting energies at 2.566 eV (green dotted line) and 2.484 eV (pink dotted line)) or the other fractions. Therefore, the splitting of energy states in the band-edge is only correlated with the mesoscale ordering of NCs into SLs, and it is not the result of quantum confinement effects. To evaluate the scattering induced by SLs in solution, we compared the relative scattering of Fraction 6 and 1-ODE NC. Both samples were excited with 420 nm light at equal concentrations, and the scattered excitation and photoluminescence were collected normal to the path of incidence. The spectra obtained for both samples are shown in Fig. 5(c), with scattered excitation observed at 420 nm for both. Our results indicated that the relative integrated scattering of the excitation beam by Fraction 6 was around 8.7 times greater than that by the 1-ODE NC sample. This increase in scattering from Fraction 6 provides further evidence supporting the observed formation of SLs in solution, as confirmed by DLS and SAXS studies.

Our structural analysis suggests that the self-assembly of NCs occurs in solution as a result of the hexane evaporation process. However, we cannot rule out other mechanisms that may lead to the formation of SLs, especially since recent reports suggest that NCs with near-ideal size distributions can become well-ordered in solution during their synthesis when local interactions favor spontaneous ordering.[48,49] Further studies will be required to determine the full mechanism, as the solvent evaporation rate, the instantaneous concentration, and NC size disparity likely affect the SL formation in the solution phase. Nonetheless, our studies suggest that NC size dispersity is an important structural parameter that must be controlled during the formation of both solution and solid-state assemblies. Samples isolated by this method also formed well-
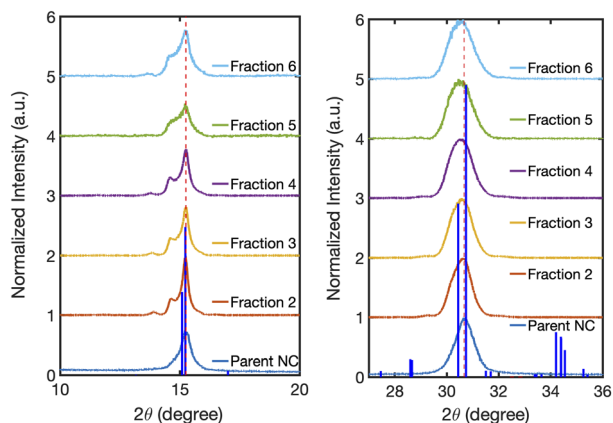
Fig. 6 Powder XRD patterns of the Parent NCs and Fractions 2–6. The XRD patterns indicate an orthorhombic crystal phase for all samples. The dotted red lines are drawn at the $2\theta = 15°$ and $30.6°$ reflection peak maxima of the Parent NCs. The XRD pattern for all the fractions shows peak splitting at $2\theta = 15°$ due to the formation of SLs.[3] The card-file for the orthorhombic crystal phase of $CsPbBr_3$ (*Pbnm*, COD 1503362) is shown in blue bars.

Fig. 7 (a) SEM image of an isolated SL of Fraction 6 deposited onto a gold substrate. (b) TEM of multiple SLs of Fraction 6 deposited onto a carbon coated copper grid.

ordered SLs in the solid state when solutions were drop-cast onto a silicon wafer substrate for powder X-ray diffraction (XRD) measurements (Fig. 6). We observed long-range structural coherence in the XRD patterns for all fractions, as evidenced by the presence of higher-order Bragg reflections. These Bragg reflections only occur if SLs made of well-defined and nearly identical NC shapes are present.[3] The Bragg reflections around the peak at $2\theta = 15°$ have been previously assigned to the (110), ($1\bar{1}0$), and (002) planes of orthorhombic $CsPbBr_3$ NCs that are close-packed in SLs.[3,16] The SL constant for each fraction was calculated as the separation distance between the (110) and ($1\bar{1}0$) planes using XRD. Our results showed SL constants of 15.4 nm, 15.1 nm, 14.4 nm, 13.1 nm, and 12.2 nm for Fraction 2, 3, 4, 5, and 6, respectively. The SL constants for Fractions 4–6 determined by SAXS (Fig. 4) are similar in magnitude to those measured through XRD and exhibit the same decreasing trend. The facile formation of solid-state SLs, like the ones measured by XRD, was further confirmed by scanning electron microscope (SEM) imaging as shown in Fig. 7(a) for a concentrated solution of Fraction 6 (30 µL with 0.8 µM concentration) drop-cast onto a gold substrate. The SLs prepared this way had an average length of 2.96 µm and width of 3.27 µm, larger than the solution-phase hydrodynamic diameter measured as peak 2 in the DLS studies shown in Fig. 3 and summarized by Table 1. The solid-state SLs were also imaged by TEM as shown in Fig. 7(b) by diluting 1 drop of the Fraction 6 stock solution with 5 drops of hexane, and then drop casting onto a carbon coated copper grid. The SLs have an average size of 100–150 nm, consistent with the average size measured by DLS for peak 2 in Fig. 3 and Table 1. Using the average size for peak 2 obtained by DLS measurements (Table 1), we estimated the size of SLs in solution for Fraction 6 to be 100 nm. Combining this with the average NC size of 8.5 nm by TEM (Fig. 3), we determined the
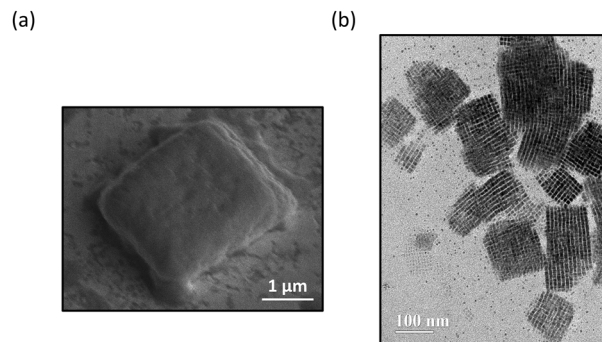
approximate number of NCs per SL to be 1600. The observed differences in the dimensions of the SLs seen in the SEM and TEM images presented in Fig. 7 may be attributed to the higher concentration of the NCs used for deposition of the film imaged by SEM. This observation suggests that the NC concentration is an important factor in determining the ordering process and formation of solid-state SLs. Ongoing studies are currently focused on controlling the size of the SLs and identifying factors that modify the formation of solid-state assemblies in thin films.

Optoelectronic response of dispersed NCs *vs.* SLs

The isolated fractions were prepared with much greater uniformity of the NC size distribution compared to a conventional synthesis protocol. Therefore, we studied Fractions 2–6 to understand how the optoelectronic properties are modified as the NC size disparity is minimized, ultimately resulting in highly ordered SLs of emitters in the solution phase. Fig. 8 summarizes the room-temperature solution phase photoluminescence lifetime of Fractions 2–6. The radiative recombination rates for the fast and slow components were determined by fitting the photoluminescence time trace to a biexponential decay,

$$\frac{I(t)}{I(0)} = \alpha_1 \, e^{-\frac{t}{\tau_1}} + \alpha_2 \, e^{-\frac{t}{\tau_2}}, \tag{1}$$

where $I(t)$ is the photoluminescence intensity at time t, $I(0)$ is the initial photoluminescence intensity, α_1 is the initial amplitude of the first exponential term, τ_1 is the lifetime of the first term, α_2 is the initial amplitude of the second exponential term, and τ_2 is the lifetime of the second term. On average, both τ_1 (fast component) and τ_2 (slow component) decreased with each subsequent fraction (Fig. 8(b) and (c), respectively). The relative contribution of each component to the measured photoluminescence decay was compared by calculating the ratio of each amplitude term, α_1 or α_2, to the sum of both amplitude terms, $\alpha_1 + \alpha_2$, as shown in Fig. 8(a). The relative contribution from the fast component (Fig. 8(a), green circles) is the dominating recombination pathway for excited carriers
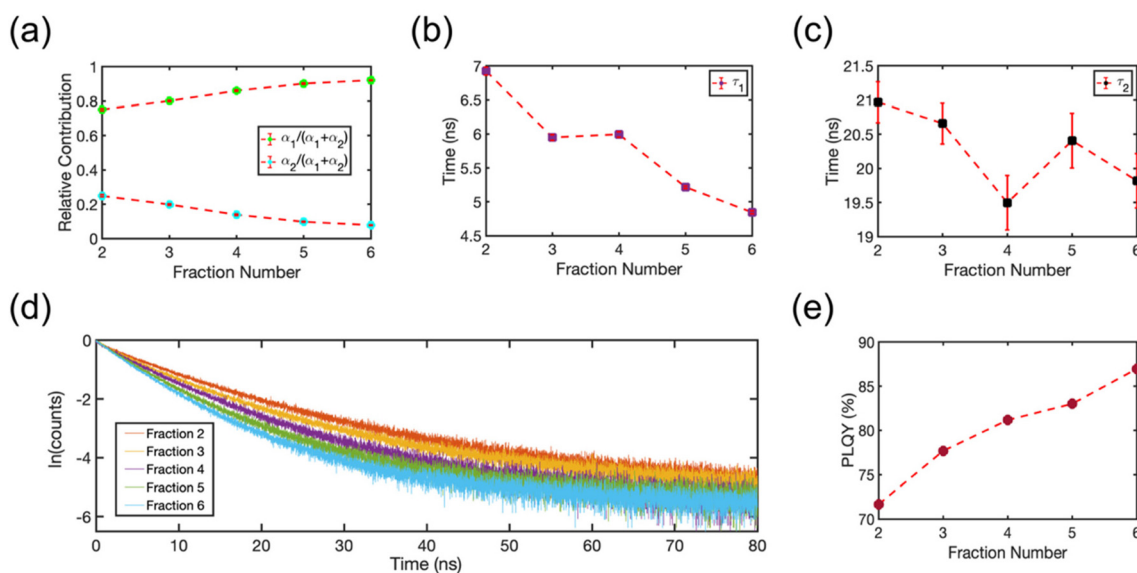
Fig. 8 (a) Relative contribution of the fast (green circles) and slow (blue circles) component of the photoluminescence decay, α_1 or α_2, for each fraction. (b) Photoluminescence lifetime of the fast component, τ_1, plotted for each fraction. (c) Photoluminescence lifetime of the slow component, τ_2, plotted for each fraction. The error bars in (a–c) are 95% confidence intervals for the fitted terms in eqn (1). (d) Photoluminescence decay signal plotted for each fraction. (e) Absolute PLQY plotted for each fraction. The photoluminescence yield increases and the photoluminescence lifetime decreases as NCs assemble into SLs.

as the NCs assemble into the SLs, while the slower recombination pathway is almost completely shut off (Fig. 8(a), blue circles).

To gain a deeper understanding of the photoluminescence decay kinetics, we measured the PLQY of the product fractions in solution. We used an integrating sphere with samples in a closed cuvette to perform the measurement at room temperature at the same concentration as the photoluminescence lifetime studies. To account for the large path-length of the integrating sphere and the spectral response of the setup, we corrected the PLQYs for any possible re-absorption effects and for the spectral response of the detection setup. Fig. 8(e) shows the absolute PLQY of the collected fractions in solution. The PLQY systematically increased with subsequent fraction number. Multiple previous studies suggest that accelerated photoluminescence decay kinetics, as reported Fig. 8(d), would be expected for NCs if the sample processing is stripping surface ligands and introducing a greater number of fast-quenching trap states that also lower PLQYs.[50,51] However, the observed improvement of PLQY is in stark contrast to this commonly observed behavior that results from conventional cleaning and isolation strategies. This trend clearly illustrates that is it possible to isolate extremely uniform CsPbBr$_3$ NCs with excellent optical properties. The isolated NCs in the early fractions and the SLs in the later fractions remained colloidally stable during structural and spectroscopic measurements and their optical quality remained constant over the course of six months when refrigerated and stored in an inert atmosphere. Further, the additional structure in the absorption spectra (Fig. 1(b)) is not due to the introduction of trap states or defects that compete with radiative recombination. Instead,

these spectral features are plausibly explained by amplified electronic coupling interactions between NCs as they form into SLs. The splitting of the exciton absorption feature into two electronic states is a result of charge delocalization in SLs made of NCs. This is especially clear in the later fractions comprised of nearly identical NCs. The two absorption peaks observed at 2.566 eV and 2.488 eV in Fraction 6 (Fig. 1(b)) represent the energy levels of the hybridized electronic states. As observed in solid-state CsPbBr$_3$ SLs, close packing of nearly identical NCs can result in the formation of minibands,[19] due to the coupling of delocalized electronic states near the band-edge. These minibands, in turn, facilitate accelerated radiative recombination dynamics. We hypothesize a similar effect is occurring in the solution-phase SLs in our studies.

Conclusion

The structural quality of CsPbBr$_3$ SLs is strongly linked to the size distribution of their constituent NCs, whereas the promising optoelectronic applications proposed for SLs also requires that the NCs maintain their defect-free electronic structure during the size-selective processing. Our results show that SLs of CsPbBr$_3$ NCs form spontaneously in solution, and that this behavior can be promoted without degrading the underlying electronic structure of the NCs. Our report is the first analysis of the optical response of solution-phase CsPbBr$_3$ SLs. Previously, SLs have only been observed in the solid state. In the solution-phase, it appears that CsPbBr$_3$ SLs exhibit unique, accelerated radiative recombination dynamics that effectively improve the radiative recombination efficiency. Our study pro-

vides additional insight into possible strategies for further enhancing radiative recombination and outcompeting the kinetics of non-radiative electronic recombination.

Conflicts of interest

The authors declare no competing financial interest.

Acknowledgements

Notes and references

1 F. Krieg, P. C. Sercel, M. Burian, H. Andrusiv, M. I. Bodnarchuk, T. Stöferle, R. F. Mahrt, D. Naumenko, H. Amenitsch and G. Rainò, *ACS Cent. Sci.*, 2020, **7**, 135–144.

2 J. S. van der Burgt, J. J. Geuchies, B. van der Meer, H. Vanrompay, D. Zanaga, Y. Zhang, W. Albrecht, A. V. Petukhov, L. Filion and S. Bals, *J. Phys. Chem. C*, 2018, **122**, 15706–15712.

3 S. Toso, D. Baranov, C. Giannini, S. Marras and L. Manna, *ACS Mater. Lett.*, 2019, **1**, 272–276.

4 K. T. Cho, S. Paek, G. Grancini, C. Roldán-Carmona, P. Gao, Y. Lee and M. K. Nazeeruddin, *Energy Environ. Sci.*, 2017, **10**, 621–627.

5 M. A. Green, A. Ho-Baillie and H. J. Snaith, *Nat. Photonics*, 2014, **8**, 506–514.

6 N. J. Jeon, J. H. Noh, Y. C. Kim, W. S. Yang, S. Ryu and S. I. Seok, *Nat. Mater.*, 2014, **13**, 897–903.

7 Y. Cao, N. Wang, H. Tian, J. Guo, Y. Wei, H. Chen, Y. Miao, W. Zou, K. Pan and Y. He, *Nature*, 2018, **562**, 249–253.

8 K. Lin, J. Xing, L. N. Quan, F. P. G. de Arquer, X. Gong, J. Lu, L. Xie, W. Zhao, D. Zhang, C. Yan, W. Li, X. Liu, Y. Lu, J. Kirman, E. H. Sargent, Q. Xiong and Z. Wei, *Nature*, 2018, **562**, 245–248.

9 M. H. Park, J. Park, J. Lee, H. S. So, H. Kim, S. H. Jeong, T. H. Han, C. Wolf, H. Lee and S. Yoo, *Adv. Funct. Mater.*, 2019, **29**, 1902017.

10 Y. Shen, L. P. Cheng, Y. Q. Li, W. Li, J. D. Chen, S. T. Lee and J. X. Tang, *Adv. Mater.*, 2019, **31**, 1901517.

11 M. A. M. Hasan, Y. Wang, C. R. Bowen and Y. Yang, *Nano-Micro Lett.*, 2021, **13**, 1–41.

12 B. J. Roman and M. T. Sheldon, *Nanophotonics*, 2019, **8**, 599–605.

13 B. J. Roman, N. M. Villegas, K. Lytle and M. Sheldon, *Nano Lett.*, 2020, **20**, 8874–8879.

14 K. Huang, K. K. Green, L. Huang, H. Hallen, G. Han and S. F. Lim, *Nat. Photonics*, 2022, **16**, 737–742.

15 S. Ortega, M. Ibáñez, Y. Liu, Y. Zhang, M. V. Kovalenko, D. Cadavid and A. Cabot, *Chem. Soc. Rev.*, 2017, **46**, 3510–3528.

16 F. Bertolotti, A. Vivani, F. Ferri, P. Anzini, A. Cervellino, M. I. Bodnarchuk, G. Nedelcu, C. Bernasconi, M. V. Kovalenko and N. Masciocchi, *Chem. Mater.*, 2022, **34**, 594–608.

17 D. D. Blach, V. A. Lumsargis, D. E. Clark, C. Chuang, K. Wang, L. Dou, R. D. Schaller, J. Cao, C. W. Li and L. Huang, *Nano Lett.*, 2022, **22**, 7811–7818.

18 E. Penzo, A. Loiudice, E. S. Barnard, N. J. Borys, M. J. Jurow, M. Lorenzon, I. Rajzbaum, E. K. Wong, Y. Liu and A. M. Schwartzberg, *ACS Nano*, 2020, **14**, 6999–7007.

19 Y. Tang, D. Poonia, M. Van Der Laan, D. Timmerman, S. Kinge, L. D. Siebbeles and P. Schall, *ACS Appl. Energy Mater.*, 2022, **5**, 5415–5422.

20 I. Cherniukh, G. Rainò, T. Stöferle, M. Burian, A. Travesset, D. Naumenko, H. Amenitsch, R. Erni, R. F. Mahrt and M. I. Bodnarchuk, *Nature*, 2021, **593**, 535–542.

21 G. Rainò, M. A. Becker, M. I. Bodnarchuk, R. F. Mahrt, M. V. Kovalenko and T. Stöferle, *Nature*, 2018, **563**, 671–675.

22 M. A. Becker, L. Scarpelli, G. Nedelcu, G. Rainò, F. Masia, P. Borri, T. Stöferle, M. V. Kovalenko, W. Langbein and R. F. Mahrt, *Nano Lett.*, 2018, **18**, 7546–7551.

23 H. Utzat, W. Sun, A. E. Kaplan, F. Krieg, M. Ginterseder, B. Spokoyny, N. D. Klein, K. E. Shulenberger, C. F. Perkinson and M. V. Kovalenko, *Science*, 2019, **363**, 1068–1072.

24 C. R. Kagan and C. B. Murray, *Nat. Nanotechnol.*, 2015, **10**, 1013–1026.

25 J. G. Bohnet, Z. Chen, J. M. Weiner, D. Meiser, M. J. Holland and J. K. Thompson, *Nature*, 2012, **484**, 78–81.

26 H. Altug, D. Englund and J. Vučković, *Nat. Phys.*, 2006, **2**, 484–488.

27 P. L. Gourley, *Sci. Am.*, 1998, **278**, 56–61.

28 Y.-J. Lu, J. Kim, H.-Y. Chen, C. Wu, N. Dabidian, C. E. Sanders, C.-Y. Wang, M.-Y. Lu, B.-H. Li and X. Qiu, Plasmonic Nanolaser Using Epitaxially Grown Silver Film, *Science*, 2012, **337**, 450–453.

29 F. Mattiotti, M. Kuno, F. Borgonovi, B. Jankó and G. L. Celardo, *Nano Lett.*, 2020, **20**, 7382–7388.

30 C. B. Murray, C. R. Kagan and M. G. Bawendi, *Annu. Rev. Mater. Sci.*, 2000, **30**, 545–610.

31 M. Nakaya, Y. Tsuchiya, K. Ito, Y. Oumi, T. Sano and T. Teranishi, *Chem. Lett.*, 2004, **33**, 130–131.

32 E. V. Shevchenko, D. V. Talapin, C. B. Murray and S. O'Brien, *J. Am. Chem. Soc.*, 2006, **128**, 3620–3637.

33 I. Coropceanu, E. M. Janke, J. Portner, D. Haubold, T. D. Nguyen, A. Das, C. P. Tanner, J. K. Utterback, S. W. Teitelbaum and M. H. Hudson, *Science*, 2022, **375**, 1422–1426.

34 M. A. Boles, M. Engel and D. V. Talapin, *Chem. Rev.*, 2016, **116**, 11220–11289.

35 J. Liu, X. Zheng, O. F. Mohammed and O. M. Bakr, *Acc. Chem. Res.*, 2022, **55**, 262–274.

36 M. Kapuscinski, P. Munier, M. Segad and L. Bergström, *Nano Lett.*, 2020, **20**, 7359–7366.

37 N. Mukharamova, D. Lapkin, I. A. Zaluzhnyy, A. André, S. Lazarev, Y. Y. Kim, M. Sprung, R. P. Kurta, F. Schreiber and I. A. Vartanyants, *Small*, 2019, **15**, 1904954.

38 J. Ye, Z. Li, D. J. Kubicki, Y. Zhang, L. Dai, C. Otero-Martínez, M. A. Reus, R. Arul, K. R. Dudipala and Z. Andaji-Garmaroudi, *J. Am. Chem. Soc.*, 2022, **144**, 12102–12115.

39 R. Babu and S. P. Singh, *Langmuir*, 2018, **34**, 15507–15516.

40 J. De Roo, M. Ibáñez, P. Geiregat, G. Nedelcu, W. Walravens, J. Maes, J. C. Martins, I. Van Driessche, M. V. Kovalenko and Z. Hens, *ACS Nano*, 2016, **10**, 2071–2081.

41 M. I. Bodnarchuk, S. C. Boehme, S. Ten Brinck, C. Bernasconi, Y. Shynkarenko, F. Krieg, R. Widmer, B. Aeschlimann, D. Günther and M. V. Kovalenko, *ACS Energy Lett.*, 2018, **4**, 63–74.

42 K. Chen, Q. Zhong, W. Chen, B. Sang, Y. Wang, T. Yang, Y. Liu, Y. Zhang and H. Zhang, *Adv. Funct. Mater.*, 2019, **29**, 1900991.

43 J. Liu, K. Song, Y. Shin, X. Liu, J. Chen, K. X. Yao, J. Pan, C. Yang, J. Yin and L.-J. Xu, *Chem. Mater.*, 2019, **31**, 6642–6649.

44 J. Liu, K. Song, X. Zheng, J. Yin, K. X. Yao, C. Chen, H. Yang, M. N. Hedhili, W. Zhang and P. Han, *J. Phys. Chem. Lett.*, 2021, **12**, 10402–10409.

45 Y. Nagaoka, K. Hills-Kimball, R. Tan, R. Li, Z. Wang and O. Chen, *Adv. Mater.*, 2017, **29**, 1606666.

46 Y. Tong, B. J. Bohn, E. Bladt, K. Wang, P. Müller-Buschbaum, S. Bals, A. S. Urban, L. Polavarapu and J. Feldmann, *Angew. Chem., Int. Ed.*, 2017, **56**, 13887–13892.

47 O. Glatter, *J. Appl. Crystallogr.*, 1980, **13**, 7–11.

48 H. Huang, M. W. Feil, S. Fuchs, T. Debnath, A. F. Richter, Y. Tong, L. Wu, Y. Wang, M. Döblinger and B. Nickel, *Chem. Mater.*, 2020, **32**, 8877–8884.

49 F. Montanarella, Q. A. Akkerman, D. Bonatz, M. M. van der Sluijs, J. C. van der Bok, P. T. Prins, M. Aebli, A. Mews, D. Vanmaekelbergh and M. V. Kovalenko, *Nano Lett.*, 2023, **23**(2), 667–676.

50 D. W. Dequilettes, K. Frohna, D. Emin, T. Kirchartz, V. Bulovic, D. S. Ginger and S. D. Stranks, *Chem. Rev.*, 2019, **119**, 11007–11019.

51 F. Xu, X. Kong, W. Wang, F. Juan, M. Wang, H. Wei, J. Li and B. Cao, *J. Alloys Compd.*, 2020, **831**, 154834.